



Bridging cell morphological behaviors and molecular dynamics in multi-modal spatial omics with MorphLink

Received: 30 June 2024

Accepted: 13 June 2025

Published online: 01 July 2025

Jing Huang ^{1,2}, Chenyang Yuan ^{1,2}, Jiahui Jiang³, Jianfeng Chen⁴, Sunil S. Badve ⁵, Yesim Gokmen-Polar ⁵, Rossana L. Segura⁶, Xinmiao Yan⁷, Alexander Lazar ^{6,7}, Jianjun Gao ⁴, Bing Yao ¹, Michael Epstein ^{1,2}, Linghua Wang ^{3,7} & Jian Hu ^{1,2}

Check for updates

Multi-modal spatial omics data are invaluable for exploring complex cellular behaviors in diseases from both morphological and molecular perspectives. Current analytical methods primarily focus on clustering and classification, and do not adequately examine the relationship between cell morphology and molecular dynamics. Here, we present MorphLink, a framework designed to systematically identify disease-related morphological-molecular interplays. MorphLink has been evaluated across a wide array of datasets, showcasing its effectiveness in extracting and linking interpretable morphological features with various molecular measurements in spatial omics analyses. These linkages provide a transparent view of cellular behavior heterogeneity within tissue regions with similar cell type compositions, characterizing tumor subtypes and immune diversity across different organs. Additionally, MorphLink is scalable and robust against cross-sample batch effects, making it an efficient method for integrative spatial omics data analysis across samples, cohorts, and modalities, and enhancing the interpretation of results for large-scale studies.

Histological images are widely used to characterize complex tissue phenotypes related to diseases. Visual inspection of biopsy specimens through histopathology has long been considered the gold standard for disease diagnosis, as disease-associated cells often exhibit distinct morphological changes, such as alterations in size, shape, and the organization of cells and extracellular matrix¹. These changes in cell morphology and the arrangement of extracellular structures can alter cells' physical capabilities, affecting their interactions with the environment, adhesion to surfaces, and migration. Complementing the analyses of morphology, high-throughput omics profiles—including mRNA expression, protein abundance, and chromatin accessibility—

provide a snapshot of the cells' functional states and their responses to environmental stimuli. The joint analysis of tissue morphology and molecular dynamics has played a pivotal role in revealing how a cell changes morphology to adapt to its function, identifying disease-related morphology-molecular relationships, and investigating the underlying causes of aberrant cellular behaviors in diseases².

Spatial omics techniques represent the latest frontier in high-throughput omics profiling³. These techniques measure diverse omics modalities while preserving their native tissue contexts. Key techniques in spatial omics include Spatial Transcriptomics (ST)⁴⁻⁶, which measures spatial mRNA abundance; spatial proteomics^{7,8}, which

¹Department of Human Genetics, School of Medicine, Emory University, Atlanta, GA, USA. ²Department of Biostatistics and Bioinformatics, Rollins School of Public Health, Emory University, Atlanta, GA, USA. ³The University of Texas MD Anderson Cancer Center UTHealth Graduate School of Biomedical Sciences (GSBS), Houston, TX, USA. ⁴Department of Gastrointestinal Medical Oncology, The University of Texas MD Anderson Cancer Center, Houston, TX, USA. ⁵Department of Pathology and Laboratory Medicine, School of Medicine, Emory University, Atlanta, GA, USA. ⁶Department of Pathology, The University of Texas MD Anderson Cancer Center, Houston, TX, USA. ⁷Department of Genomic Medicine, The University of Texas MD Anderson Cancer Center, Houston, TX, USA. e-mail: lwang22@mdanderson.org; jian.hu@emory.edu

measures highplex protein abundance; spatial CITE-seq⁹⁻¹¹, enabling the simultaneous measurement of proteins and the transcriptome; and spatial metabolomics¹² for detailed metabolite profiling. Data from these technologies is often paired with high-resolution hematoxylin and eosin-stained (H&E) images, offering cell morphology information from the same tissue slice. Such multi-modality data provide a valuable resource for linking cell morphology alterations with molecular changes. These linkages are crucial for understanding biological processes from multiple perspectives.

Several pioneering methods have been developed for the joint modeling of molecular information and histology images in spatial omics analysis. For instance, MUSE¹³ and SiGra¹⁴ utilize multi-view autoencoders to extract and combine image features with gene expression data; SpaGCN¹⁵ and SpatialGlue¹⁶ leverage undirected weighted graphs to combine molecular and image information; TESLA¹⁷ and iStar¹⁸ impute gene expression data into super-resolution gene images by leveraging high-resolution information provided by histology images. However, these methods are primarily designed for spatial domain detection by clustering and focus mainly on expression data, with histology playing a supporting role. After clustering, a common challenge is determining whether those identified spatial domains are true biological entities or just artifacts resulting from technical noise. This necessitates a post-analysis examination to assess the coherence between histological features and molecular expression within each domain. Currently, no existing methods specifically address the need to bridge gaps between morphology and molecular profiles. Efforts to assess the relationship between cell morphology and omics measurements largely depend on manual examination by pathologists¹⁹⁻²¹, which are prone to errors and inter-reader variability²²⁻²⁴. Therefore, there is a pressing need for methods that can systematically and quantitatively examine the morphology-molecular relationships in large tissue sections.

Addressing this need is non-trivial due to the following challenges: First, most analytic methods for spatial omics data rely on well-trained deep neural networks²⁵⁻²⁷ to extract hundreds of image features from histology images. Unlike genes and proteins that have clear biological meanings and functions, image features from neural networks are often not transparent, making biological interpretation difficult. Second, training such deep neural networks requires a substantial number of annotated images, leading to a labor-intensive labeling process by pathologists and inconsistent performance across different tissue types. Third, although tools like QuPath²⁸, CellVit²⁹, and Hover-Net³⁰ can extract morphology features from histology images, they primarily focus on nuclear structures and often overlook other non-nuclei structures, such as the extracellular matrix and collagen fibers, which provide complementary insights into the pathological states of tissues. As a result, these tools generate only a limited number of features, which are inadequate for linking morphology with high-dimensional molecular measurements. Lastly, there is a shortage of metrics or methods to quantify the relationship between tissue morphological and molecular measurements within a spatial context.

Here, we introduce an innovative framework, MorphLink, to address these challenges simultaneously. MorphLink has three primary goals: 1) To extract comprehensive morphological measurements with high interpretability in a label-free manner. 2) To efficiently quantify the relationships between cell morphological and molecular features in a spatial context. 3) To visually demonstrate how cellular behavior changes from both morphological and molecular perspectives. Using diverse types of spatial omics datasets, we demonstrate MorphLink's ability to efficiently extract and link various morphological hallmarks with distinct molecular measurements. These linkages facilitate a deeper understanding of cellular dynamics, which encompass the unique morphological characteristics observed within regions of similar cell type composition. Understanding these dynamics is vital for linking variations in cell morphology to their functional roles and

states. This insight is particularly critical for analyzing complex tissue properties, including tumor heterogeneity, immune diversity, and various developmental stages. Given the limited use of spatial omics in routine practice due to cost and accessibility constraints, we strongly believe that the interpretable and biologically relevant morphology features identified by MorphLink will catalyze the advancement of molecularly informed histopathology analysis, paving the way for developing accurate predictive and prognostic risk models based on histology images.

Results

Overview

We illustrate the workflow of MorphLink using ST data as an example, as it offers the most readily available and comprehensive molecular information among spatial omics techniques. However, our method is versatile and can be flexibly applied to other forms of spatial multi-omics without modifications. As shown in Fig. 1a, MorphLink begins by extracting image patches from the H&E image for measured spots in an ST tissue section. These patches then undergo spatially aware, unsupervised segmentation to generate multiple binary masks, with white pixels representing a particular structure. The properties of each mask are summarized to help users identify which cellular or extracellular structure each mask represents and the proportion of each structure across different patches. This assists users in locating dominant tissue structures and structures of interest. Summary statistics are calculated as mask-level features to quantify the distribution of these structures in each patch, capturing tissue niche layout heterogeneity. Next, connected component detection is performed within each mask to identify objects such as individual nuclei, stromal aggregates, and fiber bundles. Shape properties such as area, orientation, and solidity are measured to describe the physical attributes of each object. These object-level features complement the mask-level features, which measure tissue organization, by providing insights into sub-cellular textural morphology. As detailed in Supplementary Table 1, MorphLink can extract 10 mask-level features and 109 object-level features from each mask. Each H&E image usually has 8-10 masks, resulting in around 1,000 features that can be easily interpreted with morphological significance. Compared to the existing methods summarized in Supplementary Table 2, MorphLink provides greater flexibility and interpretability.

To understand the relationship between tissue morphology and molecular characteristics, it's essential to identify features of both modalities that share similar distribution patterns. MorphLink introduces a new statistical metric, the Curve-based Pattern Similarity Index (CPSI), as shown in Fig. 1b, to quantify the similarity of these patterns between paired features from different modalities. Our observations suggest that many features exhibit strong spatial patterns within specific tissue regions, rather than uniformly across the entire section. To capture such localized patterns when comparing similarity, the calculation of CPSI begins by partitioning the entire tissue section into subregions in a data-driven manner. In each subregion, a 2D feature pattern is broken down into changes along two orthogonal directions. Thus, the spatial pattern of each feature in the subregion is described using marginal curves along the x and y directions. The marginal similarity of a feature pair is quantified by a weighted sum of their curve correlation and difference. The subregion-level pattern similarity is then calculated as a weighted sum of their marginal similarities. Leveraging CPSI, MorphLink is able to identify features with similar spatial patterns across different modalities both locally and globally. Finally, MorphLink selects patches based on their feature values and highlights the measured structures to visually showcase what morphology features and how they change along with gene expression dynamics.

To showcase the effectiveness of MorphLink, we applied it to 8 bi- or tri-modality spatial omics datasets listed in Supplementary Table 3.

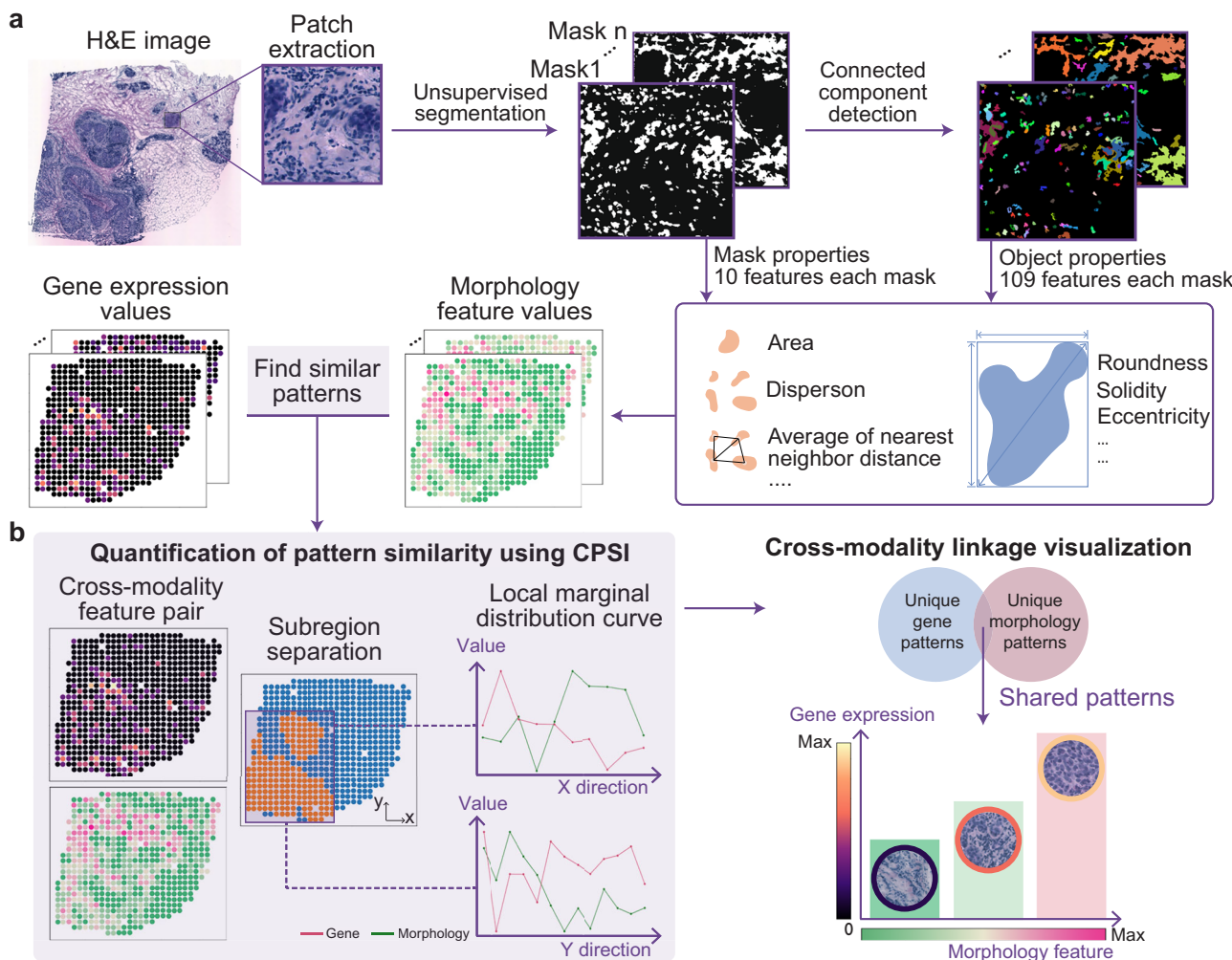


Fig. 1 | Workflow of MorphLink. **a** MorphLink starts by extracting image patches from the H&E image, then employs an unsupervised, spatially aware approach to segment each patch into multiple masks. Each mask represents a type of tissue structure, and object detection is further performed. Both mask-level and object-level summary statistics are calculated to generate interpretable image features. **b** MorphLink quantifies the pattern similarity between morphological and

molecular features by initially partitioning the tissue into subregions. Within each subregion, it calculates gradient curves along the X and Y directions to summarize the patterns of both features. The Curve-based Pattern Similarity Index (CPSI) is then computed based on these regional curves. Next, MorphLink samples patches to visually illustrate the dynamic changes in cell morphology and gene expression.

In each case, MorphLink effectively discerned multiple interpretable morphology features linked to different molecular measurements, underscoring unique cellular behaviors that drive tumor heterogeneity and immune diversity from both morphological and molecular perspectives. Additionally, we systematically evaluated the novel metric CPSI using simulated and real datasets, revealing its ability to detect spatial pattern similarities, showing greater performance over traditional metrics including correlation, structural similarity index measure (SSIM), and root mean squared error (RMSE). MorphLink's ability to analyze a broad spectrum of spatial omics data and its resilience to batch effects make it a powerful and reliable tool for transparent analysis of multi-sample spatial omics data generated from diverse studies.

Interpretable morphology features extraction

To illustrate MorphLink's ability to extract interpretable morphological features, we first analyzed a human bladder cancer ST dataset. The H&E image with pathology annotation is shown in Fig. 2a, focusing on spots enriched with tumor cells. Following the standard ST data analysis pipeline, we performed spatial clustering to delineate the tumor regions into two distinct subtypes, as shown in Fig. 2b, based on their gene expression profiles. To understand the unique expression pattern

of each region, we performed spatially variable gene (SVG) detection to identify genes that show enriched expression patterns in each tumor subtype region. Region 2 stood out with a unique expression pattern, characterized by high levels of 977 SVGs, including antigen-presenting genes (e.g., *CD74*, *B2M*, and *TAPI*) and genes associated with tumor proliferation (e.g., *MYCL*, *MKI67*, and *TUBB*), as illustrated in Fig. 2c and Supplementary Fig. 1. The elevated expression of these genes suggests that tumor cells in region 2 exhibit faster growth^{31–33} and may have enhanced antigen presentation capabilities^{34,35} which could either promote immune activation or facilitate immune evasion, thereby contributing to a more aggressive tumor phenotype. Next, we demonstrate how MorphLink captures tumor heterogeneity from a morphological perspective. Starting with spatially aware segmentation, MorphLink identifies multiple masks, detailed in Supplementary Table 4. Figure 2d shows the area proportions of these masks within tumor patches, identifying eight key structures, particularly nuclei and cancer-associated fibroblasts (CAFs), as dominant. MorphLink quantifies morphology in an interpretable manner. To visually illustrate its functionality, we selected two Visium spots from regions 1 and 2, as marked in Fig. 2b. A visual examination of Fig. 2e indicates that spot 2 has larger nuclei and a higher density of CAFs compared to spot 1. MorphLink quantifies these differences by measuring the interquartile

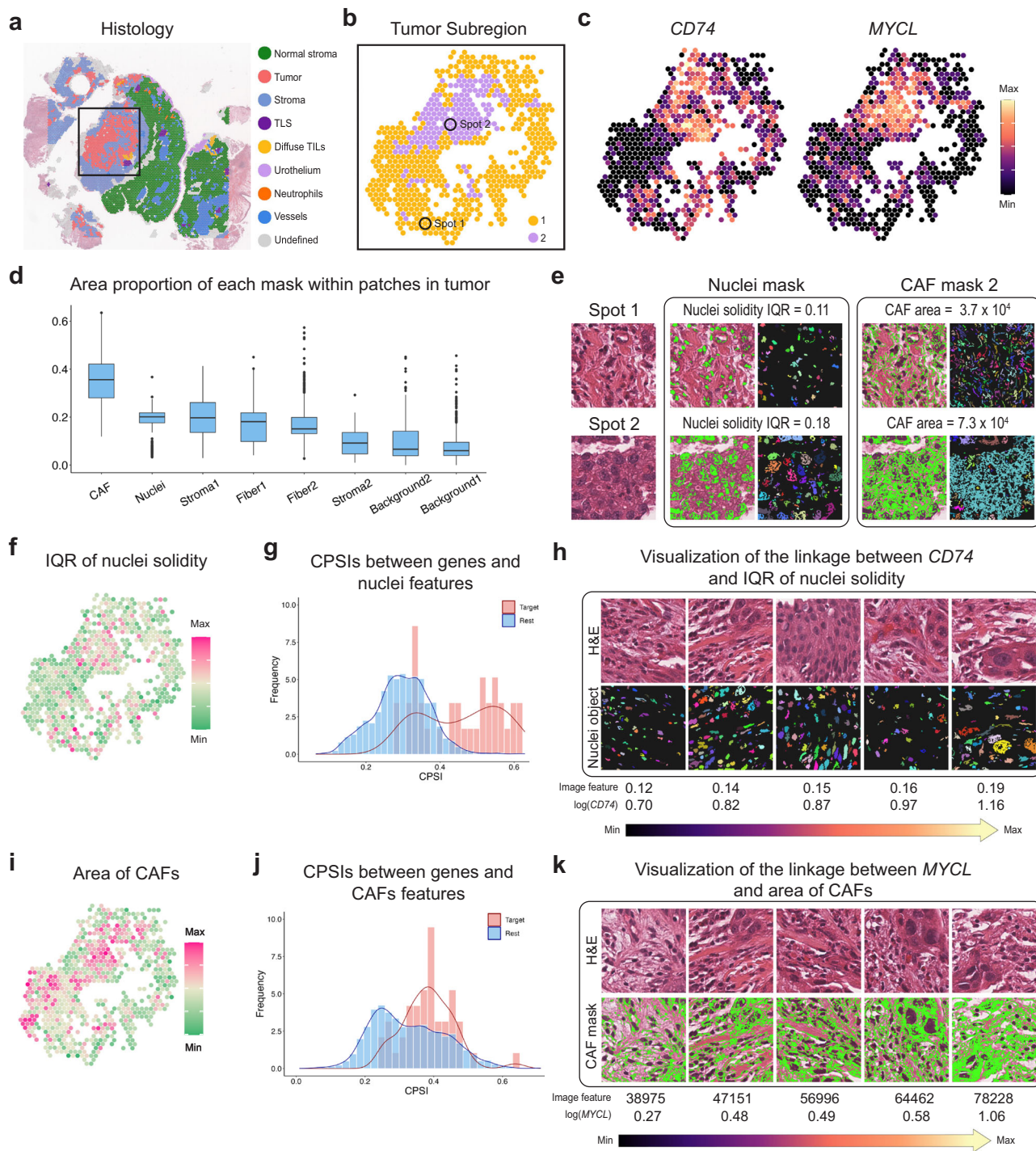


Fig. 2 | MorphLink associates nuclei and CAF morphology with gene expression to characterize tumor heterogeneity in human bladder cancer. **a** A Pathologist's annotations at the spot level overlaid on the H&E image. **b** The selected tumor region is further divided into two subregions by spatial clustering using gene expression. **c** The expression patterns of *CD74* (value range 0–2.708) and *MYCL* (value range: 0–2.708) in selected tumor regions. **d** Boxplot of the area proportion of 8 identified masks within patches in tumor regions. The lower and upper hinges correspond to the first and third quartiles, and the center refers to the median value. The upper (lower) whiskers extend from the hinge to the largest (smallest) value no further (at most) than the $1.5 \times$ interquartile range from the hinge. Data beyond the end of the whiskers is plotted individually. **e** H&E patches of two spots, with two corresponding segmented masks for nuclei and CAF; object detection is subsequently performed within each mask. **f** A morphological feature from MorphLink that quantifies the IQR of solidity for nuclei. **g** Distribution of CPSIs

between 35 antigen-presenting genes and target nuclei solidity image feature (red), compared to that between the same set of genes and other nuclei image features (blue). **h** A visual illustration of the linkage between *CD74* expression and IQR of solidity for nuclei in H&E image and detected objects. The values are median image feature values for spots stratified by *CD74*'s expression level, grouped into quantiles from 0 to 1 with a step of 0.25. **i** A morphological feature from MorphLink that quantifies the area of CAFs. **j** Distribution of CPSIs between 46 tumor proliferation-related genes and target area of CAFs image feature (red), compared to that between the same set of genes and other CAF image features (blue). **k** A visual illustration of linkages between *MYCL* expression and area of CAFs in H&E image and segmented mask. The values are median image feature values for spots stratified by *MYCL*'s expression level, grouped into quantiles from 0 to 1 with a step of 0.25.

range (IQR) of nuclei solidity (spot 1 = 0.11 vs. spot 2 = 0.18) and the area of CAFs (3.7×10^4 pixels vs. 7.3×10^4 pixels). The patterns of these two features, as presented in Fig. 2f-i, exhibit elevated values in region 2 compared to region 1.

Linking nuclei morphology with tumor antigen presentation

Studying tumor heterogeneity is critical for developing effective treatment strategies. Here, we demonstrate how MorphLink assists researchers in characterizing tumor heterogeneity by identifying linkages between molecular and morphological features. We start by examining nuclei, the dominant structure in tumor regions. As depicted in Fig. 2c and Supplementary Fig. 1, SVG analysis reveals antigen-presenting genes notably enriched in region 2. Their increased expression suggests that tumor cells in region 2 are more active in processing and presenting antigens, potentially making them more recognizable to the immune system compared to region 1, which shows lower expression levels of these molecules^{36,37}. MorphLink identified a specific morphological feature, shown in Fig. 2f, that consistently exhibits high CPSIs with antigen-presenting genes. To confirm this relationship, we identified 35 antigen-presenting genes^{38–41} in Supplementary Table 5 and compared their CPSIs with this feature and other nuclear features. A one-sided t-test yielded a *p*-value of 3.1×10^{-34} , indicating significantly higher CPSI values (Fig. 2g) and supporting the biological relevance of this pattern.

To further illustrate the connection between image features and gene expression, MorphLink used *CD74* (CPSI = 0.580) as an example to generate a visual representation in Fig. 2h. This feature measures the IQR of nuclear solidity, capturing variations in chromatin organization observed in H&E images. The compact form of DNA influences nuclear structure and size, correlating with changes in gene expression⁴². This feature increases with *CD74* expression, indicating a transition from dark, dense chromatin to more clumped and dispersed chromatin, with inconspicuous nucleoli and minimal cytoplasm. This transformation, known as the shift from heterochromatin to euchromatin, typically occurs in transcriptionally inactive regions that become transcriptionally active. The loosening and opening of chromatin are typically associated with an increase in transcriptional activity, including the activation of genes involved in antigen presentation. Previous research has demonstrated that certain genetic changes can lead to altered expression of genes regulating transcriptional activity and chromatin remodeling⁴². Consistent with these findings, our analysis revealed an enrichment of such genes in region 2 (Supplementary Fig. 2), aligning with our observations.

Linking CAF morphology with tumor proliferation

Apart from tumor cell nuclei, MorphLink also assesses tumor heterogeneity in non-nuclear structures. We emphasize the significance of these structures by highlighting the tumor proliferation status in region 2. Beyond the antigen-presenting genes mentioned earlier, another set of genes enriched in region 2, including *MYCL* (Fig. 2c), *TUBB*, and *MKI67* (Supplementary Fig. 1), are cell cycle-related genes that regulate cell growth and proliferation. Overexpression of these genes can drive uncontrolled division and growth of both tumors and CAFs, a hallmark of aggressive tumor regions^{43,44}. Identifying CAFs in H&E images represents a unique challenge because their nuclei are typically smaller, less dense, and more irregular compared to those of tumor cells and lymphocytes. Furthermore, CAFs are embedded within the stroma, a dense and complex mixture of extracellular matrix and fibers. This background can obscure the subtle characteristics of CAF nuclei, making their identification difficult with nucleus-focused image analysis tools.

MorphLink is designed to analyze broader morphological features beyond nuclei by identifying a mask that captures CAF as a dominant structure (Fig. 2d). By calculating the CPSIs between tumor proliferation genes and CAF morphology features, MorphLink identified a

feature in Fig. 2i, the area of CAF, which has the highest CPSIs with proliferation-related SVGs, including *MYCL* (CPSI = 0.637), *MKI67* (CPSI = 0.506), and *TUBB* (CPSI = 0.378). To validate this relationship, we identified 46 tumor proliferation-related genes^{45–47} (listed in Supplementary Table 5) and compared their CPSIs with this feature and other CAF features. A one-sided t-test yielded a *p*-value of 1.7×10^{-4} , indicating significantly higher CPSI values (Fig. 2j). The visual representation in Fig. 2k reveals that increased *MYCL* expression is directly linked to an expansion of the CAF region surrounding tumor cells, as highlighted in green. This expansion plays a pivotal role in supporting tumor cell growth, enhancing motility, and facilitating infiltration. This CAF-related feature, along with the nuclear chromatin changes described in our previous analysis, elucidates altered cell behaviors and highlights tumor heterogeneity in a complementary manner.

Linking lymphocyte organization with immune diversity

In addition to examining tumor heterogeneity, MorphLink can also reveal immune diversity by capturing alterations in cell organization coupled with changes in gene expression. Lymphocytes in bladder cancer tissues can be categorized as either part of tertiary lymphoid structures (TLS)⁴⁸ or as diffused tumor-infiltrating lymphocytes (TIL), as shown in Fig. 3a. SVG analysis identified *IGHM* in Fig. 3b as a distinguishing gene for these two lymphocyte organizations. *IGHM* is well-known for its critical role in lymphocyte infiltration and TLS formation⁴⁹.

To investigate immune diversity from a morphological perspective, MorphLink first identified eight major tissue structures (Fig. 3c) and then pinpointed a nuclei feature (Fig. 3d) with the highest CPSI with *IGHM* (0.483). The distribution plot in Fig. 3e shows that this feature has significantly higher CPSI values compared to other nuclear features for 28 TLS-enriched genes reported in previous studies^{50–52} in Supplementary Table 5 (one-sided t-test *p*-value = 1.0×10^{-3}). This feature measures the largest cluster size of lymphoid nuclei aggregation. Immune cells, characterized by a high nucleus-to-cytoplasm ratio, are identified in H&E images based on the arrangement of their nuclei. The size of these clusters reflects how closely lymphocytes are grouped together. Notably, this feature's value is significantly larger in TLS regions compared to diffused TIL regions (one-sided t-test, *p*-value = 3.2×10^{-9}), as demonstrated by the boxplot in Supplementary Fig. 3. The visualization provided by MorphLink in Fig. 3g also shows that in TLS, a high value of this feature indicates tightly packed lymphocyte clusters. In contrast, within diffused TIL regions, this feature has a lower value, suggesting a looser, more dispersed distribution of lymphocytes. The function and interaction of immune cells are influenced by their spatial organization. MorphLink can effectively capture these differences, offering insights into immune diversity.

In conclusion, these examples illustrate MorphLink's ability to identify morphological features in tumor cells, CAFs, and immune cells, encompassing a broad range of properties such as shape, layout, and organization. These features, closely linked to molecular dynamics, provide a comprehensive analysis of tissue morphology and its functional implications.

Application to multi-sample ST data

As spatial omics technology becomes more affordable, an increasing number of studies are producing spatial omics data from experiments designed with cohort-level sample sizes^{53–55}. Therefore, it's crucial for newly developed methods to be scalable for multi-sample analysis. To illustrate MorphLink's ability to analyze data from multiple samples, we analyzed a HER2+ human breast cancer dataset⁵³. We focused on tissue sections from patients A, H, and G, as these sections include all tumor subtypes in the original study.

For the multi-sample spatial data analysis, we first demonstrate that MorphLink effectively captures shared tissue structures across samples. We use the stromal structure as an example, as it plays a

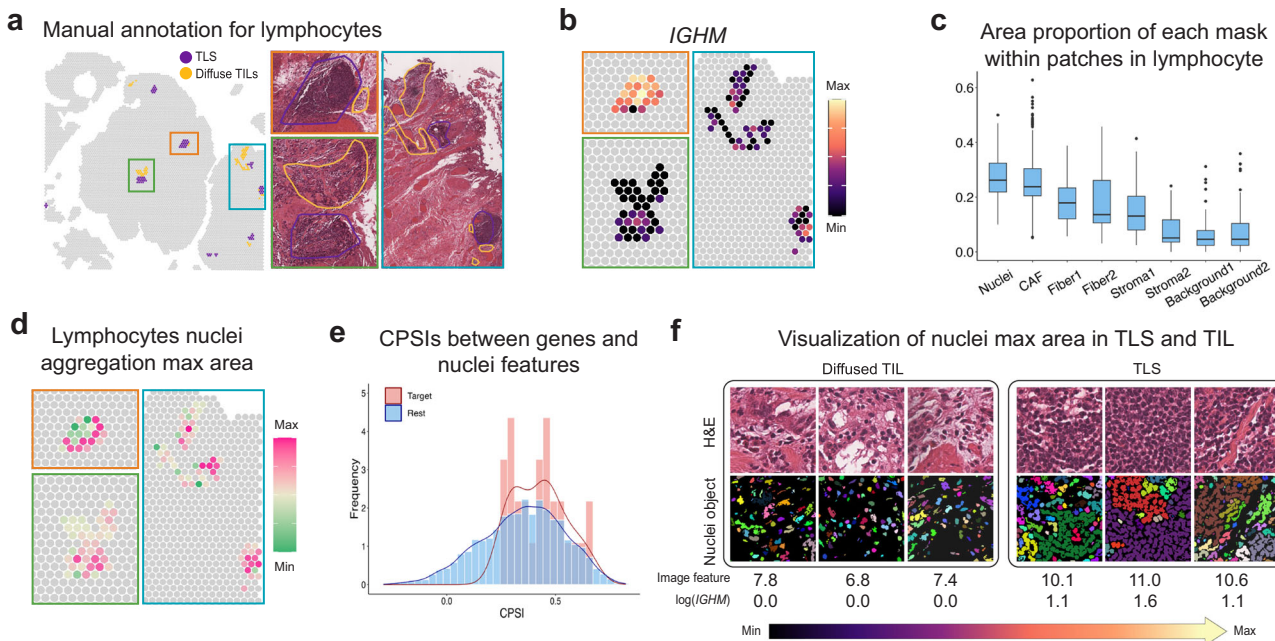


Fig. 3 | MorphLink associates lymphocyte organization with gene expression to characterize immune diversity in human bladder cancer. **a** Tertiary lymphoid structures (TLS) and diffuse tumor-infiltrating lymphocytes (TIL) annotation on spot-level and H&E image from the pathologist. **b** The expression of *IGHM* (value range: 0–2.565) at lymphocyte-enriched regions. **c** Boxplot of the area proportion of 8 identified masks within patches in lymphocyte-enriched regions. Boxplot hinges, median, and whiskers are defined the same as in Fig. 2d. **d** A morphological

feature that measures the largest cluster size of lymphoid nuclei aggregation shows high CPSIs with all TLS-enriched genes. **e** Distribution of CPSIs between 28 TLS-enriched genes and target nuclei aggregation area image feature (red), compared to that between the same set of genes and other nuclei image features (blue). **f** A visual illustration depicting how the organization of lymphocytes differs between TLS and diffused TIL in H&E images and detected nuclei.

critical role in the tumor microenvironment but is often overlooked in existing nuclei-focused morphology analyses. Our pathologist provided detailed annotations of stroma-enriched regions in the three samples, as shown in Fig. 4a. Based on the mask properties listed in Supplementary Table 6, we identified a MorphLink-derived feature—the Interquartile range (IQR) of stroma pixel distance—which consistently shows high values in the pathologist-annotated stromal regions across all three sections in Fig. 4b (one-sided two-sample t-test, A1: $p\text{-value} = 4.2 \times 10^{-24}$, G2: $p\text{-value} = 2.2 \times 10^{-30}$, H1: $p\text{-value} = 3.2 \times 10^{-31}$). This feature quantifies the variability in distances between stroma pixels, with higher values indicating greater stromal density and spatial continuity. It can also differentiate between regions of dense stroma and areas with tissue voids (Supplementary Note 1). These results highlight that MorphLink can effectively identify shared morphological patterns across multiple samples.

Next, using the regional annotations provided by the original study (Fig. 4c), we further investigated whether the extracted morphology feature displays differential patterns within tumor regions. As shown in the boxplot in Fig. 4d, this morphology feature exhibits significantly elevated values in invasive cancer compared to cancer *in situ* (one-sided two-sample t-test, A1: $p\text{-value} = 1.0 \times 10^{-2}$, G2: $p\text{-value} = 4.3 \times 10^{-2}$, H1: $p\text{-value} = 2.3 \times 10^{-7}$). These results illustrate that in invasive cancer, the stroma region not only occupies a larger proportion but also exhibits greater integration, filling more space between tumor cells compared to cancer *in situ*. The increased area and expanded presence of the stroma region are indicative of a microenvironment conducive to tumor cell growth and invasion⁵⁶. This observation points to a more aggressive and actively progressing state in the invasive tumor region compared to cancer *in situ*, highlighting the effectiveness of MorphLink in differentiating between these two stages of tumor development across multiple samples. Additionally, compared to deep neural network features, features extracted by MorphLink exhibit superior resilience to batch effects arising from variations in staining across different rounds

(Supplementary Note 2), making them better suited for multi-sample ST data analysis.

Finally, we demonstrate that our CPSI metric effectively links morphology features to differentially expressed genes enriched in invasive cancer regions. We performed differential expression analyses to identify the top 50 genes enriched in invasive cancer in each sample. We then compare the CPSI values between the target morphology feature (IQR of stroma pixel distance) and the top 50 genes, against those between the same morphology feature and all other genes. As shown in Fig. 4e, the target morphology feature has significantly higher CPSI values with the top 50 invasive cancer-enriched genes than with the remaining genes in all three samples (one-sided two-sample t-test, A1: $p\text{-value} = 2.1 \times 10^{-26}$, G2: $p\text{-value} = 1.4 \times 10^{-9}$, H1: $p\text{-value} = 3.7 \times 10^{-31}$), demonstrating the capability of CPSI in identifying meaningful molecular-morphological linkages in multi-sample analysis. A detailed case study illustrating the identified cross-sample linkages between the target morphology feature and genes enriched in invasive cancer is provided in Supplementary Note 3.

To extend MorphLink for ST data generated from different studies, managing stain color heterogeneity remains one of the main challenges. Color inconsistencies across whole slide images (WSIs) can result from various steps in WSI acquisition, including tissue cutting, fixation, staining, and scanning⁵⁷. Different acquisition parameters lead to color variations. While these parameters are usually consistent within a single laboratory, they vary across different labs. To jointly analyze multiple WSIs from different studies, staining normalization can be performed to mitigate color inconsistencies and help MorphLink better identify joint structures across WSIs (Supplementary Note 4).

Linking neuronal development with cell orientation in the mouse brain

In addition to applications in tumor analysis, we demonstrate MorphLink's utility in neurology using an adult mouse brain dataset

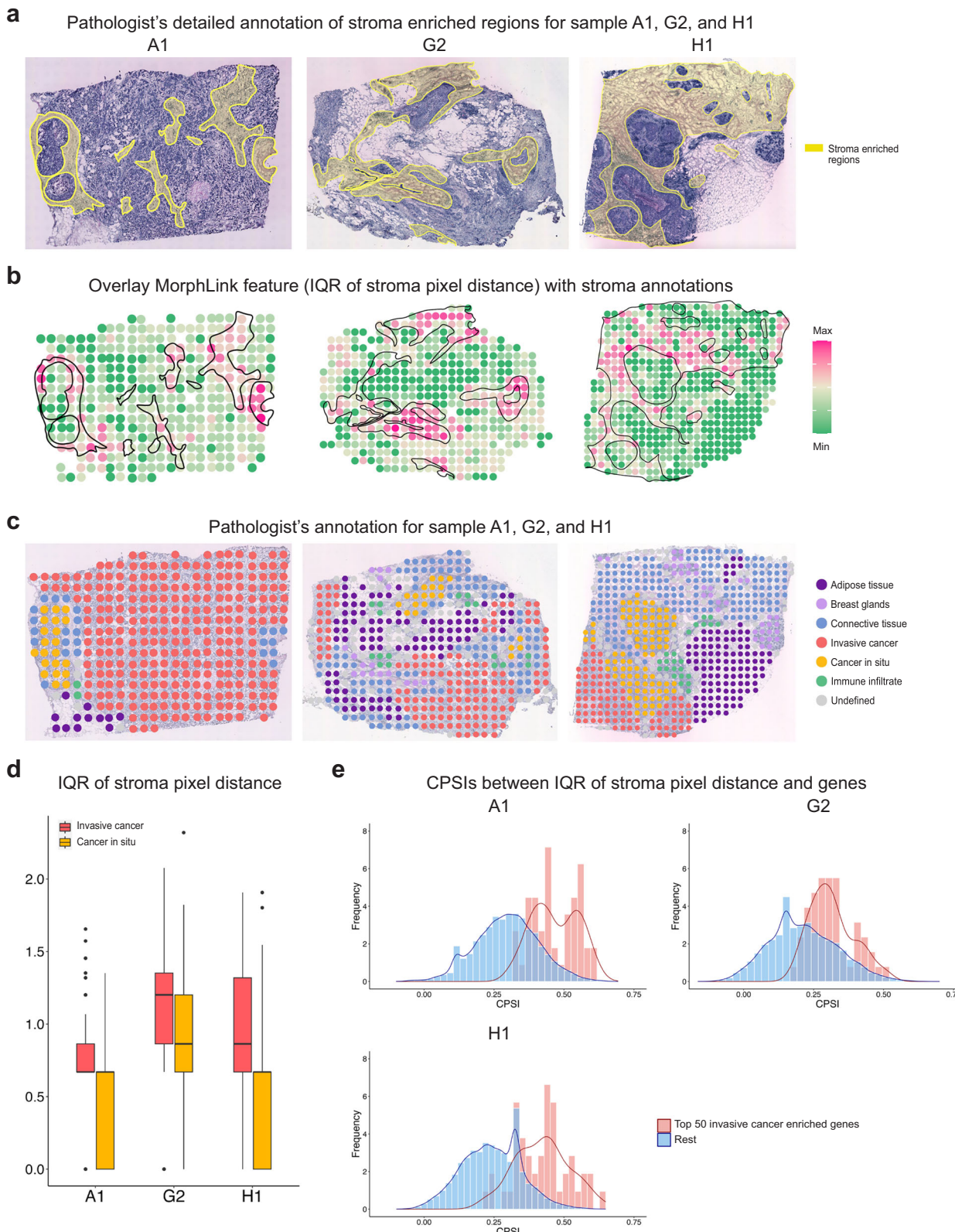


Fig. 4 | Applying MorphLink to multi-sample human breast cancer data. **a** Cellular-level stroma regions annotated by the pathologist. **b** Overlay of the extracted morphology feature (IQR of stroma pixel distance) with the pathologist-annotated stroma regions. The value ranges of the target morphology feature in the A1, G2, and H1 samples are 0–1.907, 0–2.548, and 0–2.668, respectively. **c** The manual annotations of tissue regions for samples A1, G2, and H1 by the original

study. **d** Boxplot comparing the morphology feature values in invasive cancer compared to cancer in situ across three samples (AI: $n = 282, 21$; G2: $n = 140, 20$; H1: $n = 90, 97$). Boxplot hinges, median, and whiskers are defined the same as in Fig. 2d. **e** Distribution of CPSIs between the top 50 invasive cancer-enriched genes and target morphology feature (red), compared to that between the same morphology feature and other remaining genes (blue) across three samples.

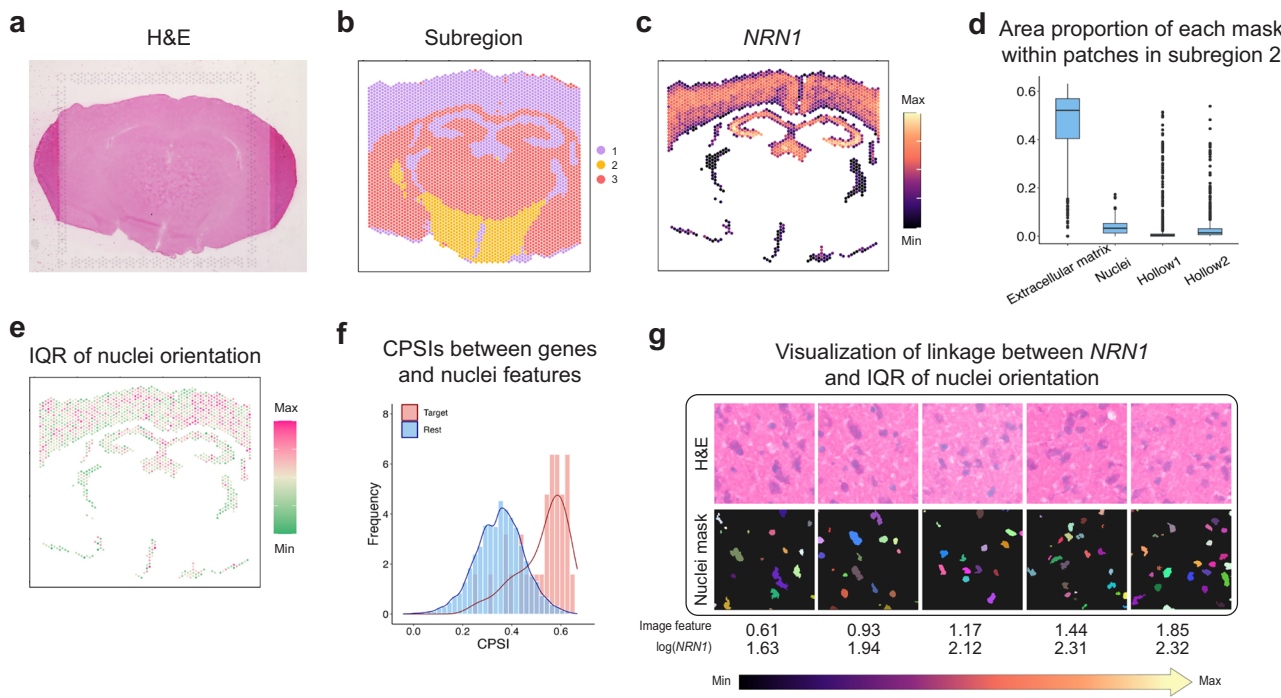


Fig. 5 | MorphLink links nuclei orientation with gene expression to characterize neuronal cell development in mouse brain data. **a** The H&E image of the mouse brain region. **b** The entire tissue region is separated into three subregions by spatial clustering using gene expression. **c** The gene expression pattern of *NRN1* in subregion 1 (value range: 0–5.631). **d** Boxplot of the area proportion of 4 identified masks within patches in subregion 1. Boxplot hinges, median, and whiskers are defined the same as in Fig. 2d. **e** A morphological feature from MorphLink

quantifies the IQR of nuclei orientation (value range: 0–2.632). **f** Distribution of CPSIs between 30 neuron development genes and target nuclei orientation image feature (red), compared to that between the same set of genes and other nuclei image features (blue). **g** A visual illustration of how neuronal cell orientation changes in H&E image and detected objects, showing a shift from the same direction to diverse directions as *NRN1* expression level increases.

from 10X Visium. The H&E image of the tissue region is displayed in Fig. 5a. MorphLink first separates the entire region into three subregions in Fig. 5b, each exhibiting strong local patterns in gene expression and image features. We specifically focus on subregion 1, which mostly corresponds to the isocortex and HPF-CA regions. Unlike tumor tissues, which often display diverse tissue structures indicated by various colors, H&E images for the brain do not contain as many distinctive tissue structures. Importantly, SVG analysis has identified a list of genes that are highly enriched in the external layer compared to the internal layers, including *NRN1* (Fig. 5c), which is related to neuron development and maturation. As summarized in Fig. 5d and Supplementary Table 7, MorphLink identified only four main strictures including nuclei, extracellular matrix, and two types of tissue hollows. It then identified a morphological feature, the IQR of nuclei's orientation, which has the highest CPSI with *NRN1* ($CPSI = 0.625$) as depicted in Fig. 5e. We also calculated the CPSIs between this image feature and 30 genes involved in the neuron development and maturation^{58–61} in Supplementary Table 5. We found that the selected image feature has significantly higher CPSIs with the gene set compared to others, as shown in Fig. 5f (one-sided two-sample t-test, $p\text{-value} = 1.46 \times 10^{-22}$).

Illustrated in Fig. 5g, this feature measures the IQR of nuclei's orientation. As *NRN1*'s expression increases, which promotes neurite outgrowth and maturation, neurons transition from the internal layers to the external layers. This image feature captures the radial migration of neuronal cells during this developmental process. Initially, neurons in the internal layers share the same orientation as they move toward the external layers. Upon completing their migration and maturing, their orientation diversifies to form sophisticated connections in various directions. This image feature effectively captures the organizational changes of neurons during their developmental process. In addition to the adult mouse brain, we also demonstrate MorphLink in an embryonic mouse brain, as shown in Supplementary Note 5.

MorphLink is robust in the presence of image artifacts

Deep learning methods for image analysis, such as ResNet⁶², HIPT²⁵, and the method by Ciga et al.⁶³ are often highly sensitive to artifacts, impacting their performance in tasks like clustering. In contrast, MorphLink demonstrates greater robustness to such artifacts. To illustrate this advantage, we analyzed the zebrafish melanoma Visium dataset⁶⁴, with the H&E image shown in Fig. 6a. This H&E image has a strong artifact of discrepancies in blurriness, which is highlighted by the red dashed line. The annotations from the original study in Fig. 6b indicate that the tissue can be largely categorized into three areas: melanoma, normal muscle, and tumor/muscle interface. For example, in our analysis of a zebrafish dataset, we noted pronounced discrepancies in blurriness across the H&E images, marked by a red dashed line in Fig. 6a. To demonstrate how this artifact affects downstream analysis, we conducted Louvain's clustering using image features derived from HIPT and MorphLink separately, and the results are shown in Fig. 6c. Notably, both the domain-detected features from HIPT and Ciga et al. display pronounced artificial effects, with the blurred region identified as cluster 1 and cluster 5, respectively. By contrast, domains detected by MorphLink features show less impact from blurriness, attributable to the robustness of its interpretable features compared to those generated by deep neural networks. Besides the melanoma region, the muscle region is less affected by artifacts.

As reported in the original study, muscle cells near the tumor exhibit distinct gene expression patterns with some example genes shown in Fig. 6d and Supplementary Fig. 4. We then demonstrate how MorphLink characterizes muscle region heterogeneity through both molecular and morphological aspects. MorphLink first identified five major structures within the muscle region, with three of them representing fiber bundles of varying colors, as shown in Fig. 6e and Supplementary Table 8. It then identified an image feature (Fig. 6f) with the

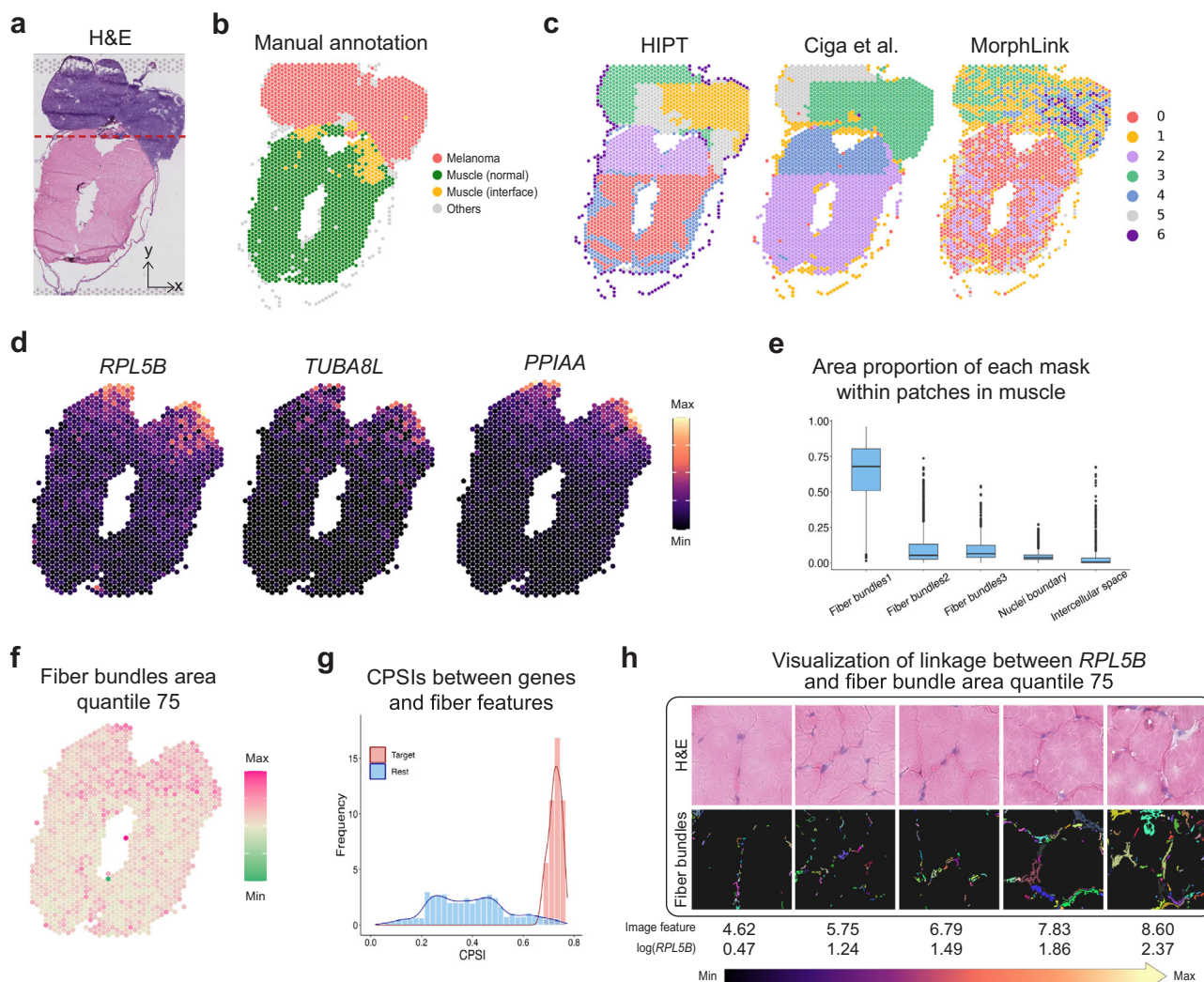


Fig. 6 | MorphLink characterizes the morphology-molecular relationship at the tumor/muscle interface. **a** The H&E image of the tissue section, with the blurred region outlined by a red dashed line. **b** Manual annotations of the tissue section from the original study. **c** Spatial domains were detected using image features derived from HIPT, Ciga et al., and MorphLink. **d** Expression patterns of *RPL5B* (value range: 0–3.367), *TUBA8L* (value range: 0–2.485), and *PPIAA* (value range: 0–3.892) in the muscle region. **e**. Boxplot of the area proportion of 5 identified masks within patches in muscle regions. Boxplot hinges, median, and whiskers are defined the same as Fig. 2d. **f** A morphological feature that quantifies the 75th

quantile of the fiber bundle area shows the highest CPSIs with *RPL5B* (0.757), *TUBA8L* (0.743), and *PPIAA* (0.747). The value for the target morphology feature is 0–8.628. **g** Distribution of CPSIs between 8 genes and target fiber bundle area image feature (red), compared to that between the same set of genes and other fiber image features (blue). **h** A visual illustration of muscle fascicle size changes associated with *RPL5B* expression in H&E image, segmented mask, and detected objects. The values are median image feature values for spot stratified by *RPL5B*'s expression level, grouped into quantiles from 0 to 1 with a step of 0.25.

highest average CPSI (0.73) across all genes enriched at the interface compared to other features (Fig. 6g, one-sided two-sample t-test, p -value = 1.34×10^{-10}). This feature measures the area of fiber bundles at the muscle boundary. Using *RPL5B* as an example, as its expression elevates, the muscle exhibits signs of cachexia at the adhesion sites, characterized by muscle atrophy due to nutrients being consumed by tumor cells⁶⁵. Consequently, the collagen degradation leads to a reduction in muscle fascicle size, resulting in more pronounced boundaries in the H&E staining in Fig. 6h. This example showcases MorphLink's capability to detect local morphology-molecular linkage even in datasets with poor-quality H&E images.

Illustration and evaluation of CPSI

A key step in MorphLink is quantifying spatial pattern similarity using our proposed metric, CPSI. CPSI produces a decimal value ranging from -1 to 1, where 1 indicates perfect similarity and -1 indicates complete dissimilarity. To illustrate how CPSI is calculated, we

provided a detailed explanation in Supplementary Note 6. To demonstrate CPSI's effectiveness in quantifying morphology and molecular feature similarities, we compared it with other commonly used metrics for pattern similarity, including correlation, SSIM, and RMSE. The results show that CPSI better captures pattern similarity than other metrics in both simulated data (Supplementary Note 7) and real data (Supplementary Note 8). Compared to the three competing metrics, CPSI's superiority is attributed to two key factors: 1) its ability to automatically separate a tissue into subregions, and 2) the high efficiency of its curve summarization method to capture spatial patterns. These advantages make CPSI a better metric to quantify multimodal feature similarity in spatial omics data.

Discussion

In this paper, we introduced MorphLink, a powerful method designed to extract, interpret, and quantify tissue morphology changes associated with molecular profiles using spatial omics data. MorphLink has

been evaluated across multiple datasets, covering various species tissues and spatial omics platforms. These results have proven its efficacy in identifying potential morphological markers that indicate molecular alterations leading to tumor heterogeneity and immune diversity. A central feature of MorphLink is CPSI, a novel metric developed for quantifying spatial pattern similarity. CPSI has consistently outperformed traditional metrics such as correlation, SSIM, and RMSE, showcasing its ability to identify features with spatial coherence across multiple modalities. The purpose of CPSI is estimation rather than inference. Due to the limited sample size in most spatial transcriptomics studies, inference is impractical. However, with a list of genes related to the same biological process, a t-test can assess if an image feature has significantly higher CPSI with these target genes compared to other features.

Compared to existing methods that rely on black box modeling, MorphLink surpasses them by providing a higher level of interpretability in spatial omics data analysis. By visually and quantitatively demonstrating the relationship between cellular morphological changes and molecular features, MorphLink allows researchers to clearly distinguish authentic biological patterns in morphology from artifacts, greatly enhancing analytical transparency. Additionally, its label-free nature and robustness against batch effects make MorphLink a superior choice for across sample and cohort data integration. To facilitate the analysis of multi-sample spatial data, within-sample feature normalization can be performed to enhance MorphLink's ability to identify shared morphology structures and their linkages with molecular features across samples. A limitation of MorphLink is that it mainly focuses on capturing local tissue morphology, in contrast to deep neural network features that capture global tissue structures. Therefore, image features from MorphLink may have limitations in clustering tasks that require the identification of global patterns.

In addition to bi-modality spatial transcriptomics data, while this study primarily showcases MorphLink's application in correlating gene expression with cell morphology in H&E-stained images, MorphLink can also be applied to tri-modality spatial omics data to establish trimodal linkages among protein abundance, gene expression, and morphology, as demonstrated in Supplementary Note 9. Beyond H&E stains, MorphLink can be applied to other histological staining techniques, such as Trichrome, Periodic Acid-Schiff (PAS), and Wright's Stain, which highlight different cellular structures and components. MorphLink's combination of versatility, interpretability, and scalability renders it an essential tool for the integration of morphology and molecular profiles in multi-sample spatial omics studies.

Methods

Input data and preprocessing

MorphLink is designed to accommodate a wide range of spatial omics and imaging data from various techniques as inputs. For molecular measurements, including mRNA, protein, or chromatin accessibility, MorphLink is capable of automatically handling raw data and performing all necessary preprocessing steps. To extract morphological features, MorphLink can handle raw histology images collected from different types of staining technologies, including Hematoxylin and Eosin (H&E) stained, Trichrome stained, microscopy, and immunofluorescence imaging.

We demonstrate the method using ST as an example. The spatial gene expression data consists of an $N \times G$ expression matrix with N spots and G genes, along with the (x, y) coordinates to record the 2-dimensional location of each spot. For gene expression and protein abundance, the expression matrix is normalized so that the abundance of each gene/protein in each spot is divided by the total abundance across all genes/proteins in that spot, multiplied by 10,000, and then transformed into a plus-one natural log scale. MorphLink can directly accept raw, high-resolution images and conduct image feature

extraction. For multi-image analysis, stain normalization using "stain-tools" is recommended to mitigate the batch effect across different staining runs.

Interpretable image feature extraction using unsupervised segmentation

Spatially aware patch segmentation. Given the typically higher resolution of histology images (pixel-level) compared to the corresponding omics data (spot-level), it is crucial to extract histological features for each spot to enable the spatial alignment of image and omics features. For each spot s in the spatial omics data, its location is represented by the 2-dimensional coordinates (x_s, y_s) . Centered on the coordinates of the spot s , MorphLink extracts a square patch with a width of m . The patch size varies with datasets generated from different techniques, and MorphLink includes a built-in function to help users determine the appropriate patch size. The patch sizes for our analyzed datasets are listed in Supplementary Table 3. Following this, we obtain a set of patches for all spots stored as a tensor with dimensions of $(N, m, m, 3)$, where N is the total number of spots. MorphLink then employs a spatially aware image segmentation method to segment each patch into multiple masks. Specifically, for each pixel v in a patch, MorphLink starts by extracting its three-channel color values (r_p, g_p, b_p) . Taking these values as features, MorphLink applies K-means clustering to divide the pixels into k clusters $\{c_1, c_2, \dots, c_k\}$, with ($k = 10$ as default). This clustering step separates pixels solely based on color value without considering spatial dependence, which may result in non-cohesive and fragile separation. To improve the spatial contiguity of separated clusters, MorphLink uses a convolution filter to refine the cluster assignments. For the pixel v assigned to the cluster $c(v)$, we identify its nearest eight pixels $\{u_1, u_2, \dots, u_8\}$ and examine their cluster assignments, denoted as $\{c(u_1), c(u_2), \dots, c(u_8)\}$. We then update the cluster assignment of the pixel v by

$$c(v)' = \begin{cases} c(v) & \text{if } \sum_{i=1}^8 I(c(u_i) = c(v)) \geq t \\ \text{mode}(\{c(u_1), c(u_2), \dots, c(u_8)\}) & \text{otherwise} \end{cases} \quad (1)$$

where $c(v)'$ denotes the updated cluster assignment of pixel v and t is a parameter to control the integrity of the clusters, with a default value of 4. This step enhances the spatial continuity of clusters by reassigning a pixel's cluster when most of its neighbors belong to a different cluster. This refinement process can be performed iteratively until more than 95% of the pixel cluster assignments remain unchanged. Although the pixel-level refinement can enhance the integrity of the segmentation, the initial total number of clusters k can be arbitrary and may result in clusters that represent non-cohesive artifacts in the image. To further improve the final clusters, MorphLink's next step is to merge the refined clusters based on their color similarity. For any two clusters $i, j \in \{1, 2, \dots, k\}$, we first calculate their color representative as the median for the Red, Green, and Blue (RGB) channels separately. Next, we define the color distance between these two clusters as

$$\text{dis}(\text{cluster}_i, \text{cluster}_j) = \max(|\text{med}(\mathbf{r}_i) - \text{med}(\mathbf{r}_j)|, |\text{med}(\mathbf{g}_i) - \text{med}(\mathbf{g}_j)|, |\text{med}(\mathbf{b}_i) - \text{med}(\mathbf{b}_j)|) \quad (2)$$

If the distance between two clusters is less than α , a predefined threshold, we proceed to merge the two clusters. This approach allows for the generation of a varying number of clusters, customized for different tissue types, ensuring substantial color differences between distinct clusters. Such customization improves the segmentation's ability to recognize hallmark structures across various tissues. An α value of 30 has been consistently effective for segmenting H&E-stained images from diverse tissue types. Subsequently, each merged cluster is

converted into a tissue mask to represent a unique biological structure.

Mask matching across-patches. The segmentation process is performed within each patch for two primary reasons. First, it allows for parallel processing and thus can be both time and memory-efficient. More importantly, segmentation at the patch level enables focused analysis on local tissue morphology. This approach contrasts with the whole slide imaging segmentation, which typically emphasizes large-scale regional distinctions, such as tumor versus non-tumor areas, but often overlooks detailed local cellular morphology. This focus on the finer details of local structure is a key distinction between the interpretable features from MorphLink and features from deep learning models.

Given that the initial segmentation is performed independently on each patch, identifying shared clusters across patches is crucial to establish common measurements for consistent tissue hallmarks. Beginning with any two random patches, labeled a and b , containing k_a and k_b clusters respectively, MorphLink examines each pair of clusters i, j between the patches, where $i \in \{1, 2, \dots, k_a\}$ and $j \in \{1, 2, \dots, k_b\}$. Utilizing the same methodology as in the cluster merging phase for determining color representativeness, we calculate the color distance $\text{dis}(\text{cluster}_i, \text{cluster}_j)$ between the two clusters. If this distance is less than a threshold of α , cluster_i and cluster_j are considered to represent the same tissue structure. This matching process is applied to all pairs of clusters between patches a and b . Following this mapping, we end up with k_{a+b} shared clusters, where $k_{a+b} \leq \min(k_a, k_b)$. These k_{a+b} clusters then serve as the basis for mapping additional patches. By applying this matching process and incorporating one more patch at a time, this approach facilitates the identification of common clusters across all patches, thereby enabling consistent measurements of identical tissue structures across the whole tissue section. In rare edge cases, clusters within a patch may be included in multiple masks, leading to redundant masks that represent the same tissue structure. To avoid this, we compare each newly generated mask with existing ones and discard it if more than half of its clusters overlap with those in any existing mask. Although mask matching may vary based on the order of patch processing, our analysis confirms that the resulting masks remain robust regardless of processing order. Additionally, we assess each mask's prevalence across all patches, excluding those that appear in fewer than 10% of patches to eliminate small debris structures that may result from artifacts.

Interpretable feature extraction. For each mask of a patch, we extract two sets of features: mask-level features and object-level features. Mask-level features aim to quantify the distribution of white pixels in each mask. Additionally, we perform a distance transformation on both white and black pixels in each mask and utilize summary statistics to characterize their distributions. To extract object-level features, we perform connected component detection on each mask of a patch using the Spaghetti algorithm. This procedure identifies individual objects within the masks, such as single nuclei or stromal aggregations. Following the detection of these objects, we measure the shape properties of each object within a patch mask. Given the numerous objects detected from each patch, we compile summary statistics for each property to obtain single-value measurements. These measurements include mean, median, interquartile range (IQR), standard deviation, and quantiles (ranging from 0 to 1 in steps of 0.25). A comprehensive description of extracted image features is listed in Supplementary Table 1. Some features may measure similar properties or provide complementary perspectives. The reason for including these features is to capture a broader and more comprehensive range of patterns, thereby enabling more precise interpretations and implications for downstream analyses.

Selective-log transformation. The interpretable image features vary widely in scales and distributions. For instance, features quantifying the area of masks might range from 0 to 10^4 pixels, whereas the solidity of objects fluctuates between 0 and 1. Inspired by the pre-processing steps used in gene expression data, MorphLink applies a selective log transformation to morphology features to enhance their normality and informativity. For any given feature, we initially adjust it to a non-negative range by subtracting its minimum value. Following this, we apply a plus-one log transformation. We then assess the standard deviation of this feature before and after this log transformation to decide whether the transformation should be retained. Specifically, for a feature f , we first normalize it to the $[0, 1]$ range and then compute its standard deviation as std_f . Alternatively, we apply a plus-one log transformation on the feature values and then normalize the logged values back to the $[0, 1]$ range. The standard deviation is recalculated as $\text{std}_{\log(f+1)}$. If $\text{std}_{\log(f+1)} > \text{std}_f$, indicating increased variance, we proceed with the plus-one log transformation for that feature. This transformation makes the distribution of image features similar to that of molecular measurements, enabling further comparison.

Similarity measurement using CPSI

Subregion division. Our observations have revealed that many features display strong spatial pattern similarities within specific tissue subregions, rather than uniformly across the entire section. Quantifying these patterns on a whole-section scale could potentially dilute these localized patterns. Hence, our approach with MorphLink begins by partitioning the entire tissue section into subregions. This separation ensures that gene expression and image features overall share a higher degree of spatial pattern similarity within each subregion than across subregions. To achieve this separation, we first employ PCA dimension reduction, retaining the top 50 PCs, and then perform Louvain clustering on image features and gene expression separately. For each modality, we set the resolution to generate 5-10 clusters. The number of initial clusters will not sensitively affect the following merging of subregions (Supplementary Note 10). Then the spots are divided into I sets by image features (modality 1), represented as $\{s_{11}, s_{12}, \dots, s_{1I}\}$, and into J sets by gene expression (modality 2), represented as $\{s_{21}, s_{22}, \dots, s_{2J}\}$. Using the Jaccard index to evaluate the overlapping between cluster pairs, if any cluster pair with $i \in \{1, 2, \dots, I\}$ and $j \in \{1, 2, \dots, J\}$

$$\frac{n(s_{1i} \cap s_{2j})}{n(s_{1i} \cup s_{2j})} > \beta \quad (3)$$

MorphLink proceeds to merge these clusters. To efficiently manage multiple overlapping clusters that need merging, we sort the cluster pairs by their overlapping ratios in descending order. Then the merging process begins from the highest ratio and continues until all clusters are examined, resulting in K subregions. By default, the threshold value for β is set at 0.2, facilitating a strategic balance in the integration of clusters. To note, subregion partitioning is optional when pathologists' annotations are available, as region separation by pathologists tends to be more biologically significant and clinically relevant.

Calculating marginal curves. For a feature f within a subregion, MorphLink first normalizes its value to $[0, 1]$, and then generates two curves to capture the spatial pattern's gradient changes along two orthogonal directions, i.e., X and Y. To analyze the feature gradient changes along, e.g., X direction, we first apply a window size of l to divide the subregion into t_x intervals of equal length, calculated as

$$t_x = \left\lceil \frac{\max(x) - \min(x)}{l} \right\rceil \quad (4)$$

where t_x denotes the number of intervals along X-axis. For each interval, we calculate the median feature value of the spots that fall within it. This process produces a vector of length t_x representing marginal distribution along the x-axis, denoted as

$$\text{curve}_x = (m_{1x}, m_{2x}, \dots, m_{t_x x}) \quad (5)$$

where m_{ix} denotes the median feature value of i^{th} interval along X-axis, $i \in \{1, 2, \dots, t_x\}$. The same procedure is applied to the Y-axis to generate a curve vector of length t_y . The window size l is the only parameter in this calculation. Rather than setting a fixed value for l , we control the minimum value of t_x and t_y to ensure summary curves capture detailed patterns to a sufficient extent. The value of l is then determined by setting $\min(t_x, t_y)$ equals 100, which has consistently yielded good performances across all analyzed datasets.

Quantification of curve-based similarity. For any two features \mathbf{f}_1 and \mathbf{f}_2 , the regional pattern similarity can be calculated as a weighted sum of marginal similarities

$$\text{CPSI}(\mathbf{f}_1, \mathbf{f}_2) = w \times \text{Similarity along X} + (1 - w) \times \text{Similarity along Y} \quad (6)$$

where the marginal similarity along the X is quantified by the sum of curve correlation and the inverse of the absolute difference

$$\text{Similarity along X} = \rho(\text{curve}_{1x}, \text{curve}_{2x}) + \left(1 - \frac{\|\text{curve}_{1x} - \text{curve}_{2x}\|_1}{t_x}\right) \quad (7)$$

and w is a weight parameter determined by

$$w = \frac{t_x}{t_x + t_y} \quad (8)$$

The marginal similarity along the Y can be quantified in the same way. Next, the global CPSI can be derived by a summation of local CPSIs weighed by the size of each subregion:

$$\text{Global CPSI}(\mathbf{f}_1, \mathbf{f}_2) = \sum_{k=1}^K \frac{C(s_k)}{N} \times \text{CPSI}_k(\mathbf{f}_1, \mathbf{f}_2) \quad (9)$$

where $C(s_k)$ represents the number of spots within the subregion k (i.e., s_k) and N is the total number of spots in the dataset.

To clarify, our interpretation of spatial pattern similarity focuses on the structural arrangement rather than absolute values, measuring the degree to which two features partition space in a similar manner.

Sample selection for visual demonstrations

For a pair of morphology feature \mathbf{f} and gene expression \mathbf{g} that have a high CPSI, MorphLink provides a visual demonstration of how tissue morphology changes with alterations in gene expression. To accomplish this, MorphLink initially stratifies all the spots into 5 groups based on the quantiles of their \mathbf{g} expression. Subsequently, it focuses on the tissue masks where feature \mathbf{f} is measured. The process begins with sorting all the patches in each group based on the area of the target region in each patch, and then selecting those patches whose mask area falls within the 25th and 75th quantiles. This step ensures that the patches chosen for display are proportionally representative of the measured structure. Finally, MorphLink selects the patches with the median \mathbf{f} value within each group as a representative sample, providing a clear visualization of the relationship between \mathbf{f} and \mathbf{g} . Due to variations in staining and the complexity of tissue morphology, assigning precise labels to identified tissue structures often requires users' specialized domain knowledge. To facilitate a better understanding of measured structures, MorphLink summarizes the

characteristic properties of each mask and provides representative patch examples, enabling users to generate more accurate interpretations.

Reporting summary

Further information on research design is available in the Nature Portfolio Reporting Summary linked to this article.

Data availability

We analyzed six spatial transcriptomics data and one spatial CITE-seq data. Publicly available data were acquired from the following websites or accession numbers: (1) human bladder tumor 10x Visium data (GEO repository: [GSE246011](https://www.ncbi.nlm.nih.gov/geo/query/acc.cgi?acc=GSE246011)); (2) zebrafish melanoma 10x Visium data (GEO repository: [GSE159709](https://www.ncbi.nlm.nih.gov/geo/query/acc.cgi?acc=GSE159709)); (3) human tonsil spatial CITE-seq data (<https://www.10xgenomics.com/datasets/gene-protein-expression-library-of-human-tonsil-cytassist-ffppe-2-standard>); (4) human HER2-positive breast tumor spatial transcriptomics data (<https://github.com/almaan/her2st>); (5) human breast tumor 10x Visium data (<https://www.10xgenomics.com/datasets/human-breast-cancer-visium-fresh-frozen-whole-transcriptome-1-standard>); (6) mouse brain 10x Visium data (<https://www.10xgenomics.com/datasets/fresh-frozen-visium-on-cytassist-mouse-brain-probe-based-whole-transcriptome-profiling-2-standard>); (7) mouse embryo 10x Visium data (<https://www.10xgenomics.com/datasets/visium-cytassist-mouse-embryo-11-mm-capture-area-ffpe-2-standard>); (8) human breast tumor H&E images from TCGA data (<https://portal.gdc.cancer.gov/> sample ID: DXL01FB49CC, DXL1.392580F3, DXL1OE26C46D). Details of the datasets analyzed in this paper are described in Supplementary Table 3.

Code availability

An open-source implementation of the MorphLink algorithm can be downloaded from GitHub: <https://github.com/jianhuupenn/MorphLink>.

References

1. Fitzgibbons, P. L. et al. Prognostic factors in breast cancer: College of American Pathologists consensus statement 1999. *Arch. Pathol. Lab. Med.* **124**, 966–978 (2000).
2. Ash, J. T. et al. Joint analysis of expression levels and histological images identifies genes associated with tissue morphology. *Nat. Commun.* **12**, 1609 (2021).
3. Vandereyken, K. et al. Methods and applications for single-cell and spatial multi-omics. *Nat. Rev. Genet.* **24**, 494–515 (2023).
4. Chen, K. H. et al. Spatially resolved, highly multiplexed RNA profiling in single cells. *Science* **348**, aaa6090 (2015).
5. Stickels, R. R. et al. Highly sensitive spatial transcriptomics at near-cellular resolution with Slide-seqV2. *Nat. Biotechnol.* **39**, 313–319 (2021).
6. Eng, C.-H. L. et al. Transcriptome-scale super-resolved imaging in tissues by RNA seqFISH+. *Nature* **568**, 235–239 (2019).
7. Black, S. et al. CODEX multiplexed tissue imaging with DNA-conjugated antibodies. *Nat. Protoc.* **16**, 3802–3835 (2021).
8. Keren, L. et al. MIBI-TOF: a multiplexed imaging platform relates cellular phenotypes and tissue structure. *Sci. Adv.* **5**, eaax5851 (2019).
9. Liu, Y. et al. High-plex protein and whole transcriptome co-mapping at cellular resolution with spatial CITE-seq. *Nat. Biotechnol.* **41**, 1405–1409 (2023).
10. Liao, S. et al. Integrated spatial transcriptomic and proteomic analysis of fresh frozen tissue based on stereo-seq. *bioRxiv* (2023).
11. Ben-Chetrit, N. et al. Integration of whole transcriptome spatial profiling with protein markers. *Nat. Biotechnol.* **41**, 788–793 (2023).
12. Vicari, M. et al. Spatial multimodal analysis of transcriptomes and metabolomes in tissues. *Nat. Biotechnol.* **42**, 1046–1050 (2024).
13. Bao, F. et al. Integrative spatial analysis of cell morphologies and transcriptional states with MUSE. *Nat. Biotechnol.* **40**, 1–10 (2022).

14. Tang, Z. et al. SiGra: single-cell spatial elucidation through an image-augmented graph transformer. *Nat. Commun.* **14**, 5618 (2023).
15. Hu, J. et al. SpaGCN: Integrating gene expression, spatial location and histology to identify spatial domains and spatially variable genes by graph convolutional network. *Nat. Methods* **18**, 1342–1351 (2021).
16. Long, Y. et al. Deciphering spatial domains from spatial multi-omics with SpatialGlue. *Nat. Methods* **2024**, *21*, 1658–1667.
17. Hu, J. et al. Deciphering tumor ecosystems at super resolution from spatial transcriptomics with TESLA. *Cell Syst.* **14**, 404–417.e4 (2023).
18. Zhang, D. et al. Inferring super-resolution tissue architecture by integrating spatial transcriptomics with histology. *Nat. Biotechnol.* **42**, 1–6 (2024).
19. Haghghi, M. et al. High-dimensional gene expression and morphology profiles of cells across 28,000 genetic and chemical perturbations. *Nat. Methods* **19**, 1550–1557 (2022).
20. Vaynberg, J. et al. Structure of an ultraweak protein-protein complex and its crucial role in regulation of cell morphology and motility. *Mol. cell* **17**, 513–523 (2005).
21. Attri, P. et al. Impact of atmospheric pressure plasma treated seeds on germination, morphology, gene expression and biochemical responses. *Jpn. J. Appl. Phys.* **60**, 040502 (2021).
22. Corredor, G. et al. Spatial architecture and arrangement of tumor-infiltrating lymphocytes for predicting likelihood of recurrence in early-stage non-small cell lung cancer. *Clin. Cancer Res.* **25**, 1526–1534 (2019).
23. Corredor, G. et al. An imaging biomarker of tumor-infiltrating lymphocytes to risk-stratify patients with HPV-associated oropharyngeal cancer. *J. Natl. Cancer Inst.* **114**, 609–617 (2022).
24. Corredor, G. et al. A review of AI-based radiomics and computational pathology approaches in triple-negative breast cancer: current applications and perspectives. *Clin. Breast Cancer* **23**, 800–812 (2023).
25. Chen, R. J. et al. Scaling Vision Transformers to Gigapixel Images via Hierarchical Self-Supervised Learning. In *Proc. IEEE/CVF Conference on Computer Vision and Pattern Recognition*. (IEEE, 2022).
26. Dosovitskiy, A. et al. An image is worth 16x16 words: transformer for image recognition at scale. *arXiv preprint arXiv:2010.11929* (2020).
27. Wang, S. et al. Computational staining of pathology images to study the tumor microenvironment in lung cancer. *Cancer Res.* **80**, 2056–2066 (2020).
28. Bankhead, P. et al. QuPath: Open source software for digital pathology image analysis. *Sci. Rep.* **7**, 1–7 (2017).
29. Hörist, F. et al. Cellvit: vision transformers for precise cell segmentation and classification. *Med. Image Anal.* **103143** (2024).
30. Graham, S. et al. Hover-Net: simultaneous segmentation and classification of nuclei in multi-tissue histology images. *Med. Image Anal.* **58**, 101563 (2019).
31. Rickman, D. S., Schulte, J. H. & Eilers, M. The expanding world of N-MYC-driven tumors. *Cancer Discov.* **8**, 150–163 (2018).
32. Wu, C. C. et al. High-resolution ribosome profiling defines discrete ribosome elongation states and translational regulation during cellular stress. *Mol. Cell* **73**, 959–970.e5 (2019).
33. Wahlström, T. & Henriksson, M. A. Impact of MYC in regulation of tumor cell metabolism. *Biochim. Biophys. Acta Gene Regul. Mechan.* **1849**, 563–569 (2015).
34. Wang, J. et al. Identification of immune cell infiltration and diagnostic biomarkers in unstable atherosclerotic plaques by integrated bioinformatics analysis and machine learning. *Front. Immunol.* **13**, 956078 (2022).
35. Basha, G. et al. A CD74-dependent MHC class I endolysosomal cross-presentation pathway. *Nat. Immunol.* **13**, 237–245 (2012).
36. Goerdts, S. & Orfanos, C. E. Other functions, other genes: alternative activation of antigen-presenting cells. *Immunity* **10**, 137–142 (1999).
37. van den Elsen, P. J. et al. Transcriptional regulation of antigen presentation. *Curr. Opin. Immunol.* **16**, 67–75 (2004).
38. Santambrogio, L., Berendam, S. J. & Engelhard, V. H. The antigen processing and presentation machinery in lymphatic endothelial cells. *Front. Immunol.* **10**, 1033 (2019).
39. Kelly, A. & Trowsdale, J. Genetics of antigen processing and presentation. *Immunogenetics* **71**, 161–170 (2019).
40. Thompson, J. C. et al. Gene signature of antigen processing and presentation machinery predicts response to checkpoint blockade in non-small cell lung cancer (NSCLC) and melanoma. *J. Immunother. Cancer* **8** (2020).
41. Gkountidi, A. O. et al. MHC class II antigen presentation by tumoral lymphatics is required for tumor specific signature and suppressive functions of Tregs. *Cancer Immunol. Res.* **9**, 748 (2021).
42. Zink, D., Fischer, A. H. & Nickerson, J. A. Nuclear structure in cancer cells. *Nat. Rev. Cancer* **4**, 677–687 (2004).
43. Xing, F., Saidou, J. & Watabe, K. Cancer associated fibroblasts (CAFs) in tumor microenvironment. *Front. Biosci. J. Virtual Libr.* **15**, 166 (2010).
44. Sahai, E. et al. A framework for advancing our understanding of cancer-associated fibroblasts. *Nat. Rev. Cancer* **20**, 174–186 (2020).
45. Whitfield, M. L. et al. Common markers of proliferation. *Nat. Rev. Cancer* **6**, 99–106 (2006).
46. Sack, L. M. et al. Profound tissue specificity in proliferation control underlies cancer drivers and aneuploidy patterns. *Cell* **173**, 499–514.e23 (2018).
47. Stein, J. P. et al. Prognostic markers in bladder cancer: a contemporary review of the literature. *J. Urol.* **160**, 645–659 (1998).
48. Sautes-Fridman, C. et al. Tertiary lymphoid structures in the era of cancer immunotherapy. *Nat. Rev. Cancer* **19**, 307–325 (2019).
49. Hao, D. et al. The single-cell immunogenomic landscape of B and plasma cells in early-stage lung adenocarcinoma. *Cancer Discov.* **12**, 2626–2645 (2022).
50. Wang, X.-X. et al. Identifying specific TLS-associated genes as potential biomarkers for predicting prognosis and evaluating the efficacy of immunotherapy in soft tissue sarcoma. *Front. Immunol.* **15**, 1372692 (2024).
51. Wu, S. et al. Multi-omics profiling and experimental verification of tertiary lymphoid structure-related genes: molecular subgroups, immune infiltration, and prognostic implications in lung adenocarcinoma. *Front. Immunol.* **15**, 1453220 (2024).
52. Ma, Y. et al. Integrating tertiary lymphoid structure-associated genes into computational models to evaluate prognostication and immune infiltration in pancreatic cancer. *J. Leukoc. Biol.* **116**, 589–600 (2024).
53. Andersson, A. et al. Spatial deconvolution of HER2-positive breast cancer delineates tumor-associated cell type interactions. *Nat. Commun.* **12**, 6012 (2021).
54. Shi, H. et al. Spatial atlas of the mouse central nervous system at molecular resolution. *Nature* **622**, 552–561 (2023).
55. Maynard, K. R. et al. Transcriptome-scale spatial gene expression in the human dorsolateral prefrontal cortex. *Nat Neurosci.* **24**, 425–436 (2021).
56. Li, H., Fan, X. & Houghton, J. Tumor microenvironment: the role of the tumor stroma in cancer. *J. Cell. Biochem.* **101**, 805–815 (2007).
57. Marini, N. et al. Data-driven color augmentation for H&E stained images in computational pathology. *J. Pathol. Inform.* **14**, 100183 (2023).
58. Nadarajah, B. & Parnavelas, J. G. Modes of neuronal migration in the developing cerebral cortex. *Nat. Rev. Neurosci.* **3**, 423–432 (2002).
59. Linker, S. B. et al. Human-specific regulation of neural maturation identified by cross-primate transcriptomics. *Curr. Biol.* **32**, 4797–4807.e5 (2022).

60. He, Z. & Yu, Q. Identification and characterization of functional modules reflecting transcriptome transition during human neuron maturation. *BMC Genomics* **19**, 1–11 (2018).
61. Brazert, M. et al. Expression of genes involved in neurogenesis, and neuronal precursor cell proliferation and development: novel pathways of human ovarian granulosa cell differentiation and transdifferentiation capability in vitro. *Mol. Med. Rep.* **21**, 1749–1760 (2020).
62. He, K. et al. Deep residual learning for image recognition. *IEEE Conference on Computer Vision and Pattern Recognition*. 770–778 (IEEE, 2016).
63. Ciga, O., Xu, T. & Martel, A. L. Self supervised contrastive learning for digital histopathology. *Mach. Learn. Appl.* **7**, 100198 (2022).
64. Hunter, M. V. et al. Spatially resolved transcriptomics reveals the architecture of the tumor-microenvironment interface. *Nat. Commun.* **12**, 6278 (2021).
65. Siff, T. et al. Cancer-mediated muscle cachexia: Etiology and clinical management. *Trends Endocrinol. Metab.* **32**, 382–402 (2021).

Acknowledgements

J.Hu. was fully supported by start-up funds from the Department of Human Genetics, School of Medicine at Emory University. L.W. was supported in part by the NIH/NCI grants R01CA266280, U24CA274274, the Break Through Cancer Foundation, and the University of Texas MD Anderson Cancer Center Institutional Research Grant (IRG) Program. We thank N. Ma for the workflow figure design and generation.

Author contributions

This study was conceived of and led by J. Hu. J. Hu and J. Huang designed the model and algorithm. J. Huang implemented the Morph-Link software and led the analysis with evaluation input from S.S.B., Y.G.P., L.W., B.Y., and M.E. J.C., J.G., X.Y., R.L.S., and A.L. generated and annotated the human bladder tumor data. C.Y. and J.J. contributed to figure generation. J.Hu and J. Huang wrote the paper with feedback from all other coauthors.

Competing interests

This study was supported by start-up research funds from the Department of Human Genetics, School of Medicine at Emory University. The authors declare no competing interests.

Additional information

Supplementary information The online version contains supplementary material available at <https://doi.org/10.1038/s41467-025-61142-0>.

Correspondence and requests for materials should be addressed to Linghua Wang or Jian Hu.

Peer review information *Nature Communications* thanks the anonymous reviewer(s) for their contribution to the peer review of this work. A peer review file is available.

Reprints and permissions information is available at <http://www.nature.com/reprints>

Publisher's note Springer Nature remains neutral with regard to jurisdictional claims in published maps and institutional affiliations.

Open Access This article is licensed under a Creative Commons Attribution-NonCommercial-NoDerivatives 4.0 International License, which permits any non-commercial use, sharing, distribution and reproduction in any medium or format, as long as you give appropriate credit to the original author(s) and the source, provide a link to the Creative Commons licence, and indicate if you modified the licensed material. You do not have permission under this licence to share adapted material derived from this article or parts of it. The images or other third party material in this article are included in the article's Creative Commons licence, unless indicated otherwise in a credit line to the material. If material is not included in the article's Creative Commons licence and your intended use is not permitted by statutory regulation or exceeds the permitted use, you will need to obtain permission directly from the copyright holder. To view a copy of this licence, visit <http://creativecommons.org/licenses/by-nc-nd/4.0/>.

© The Author(s) 2025